HHS Public Access

Author manuscript

NMR Biomed. Author manuscript; available in PMC 2024 January 01.

Published in final edited form as:

NMR Biomed. 2023 January ; 36(1): e4816. doi:10.1002/nbm.4816.

Comparison of Two Types of Microscopic Diffusion Anisotropy in Mouse Brain

Jens H. Jensen[1,2,3,*], **Josh Voltin**[1,2], **Xingju Nie**[1,2], **Siddhartha Dhiman**[2], **Emile T. McKinnon**[2], **Maria F. Falangola**[1,2]

[1]Center for Biomedical Imaging, Medical University of South Carolina, Charleston, SC, USA

[2]Department of Neuroscience, Medical University of South Carolina, Charleston, SC, USA

[3]Department of Radiology and Radiological Science, Medical University of South Carolina, Charleston, SC, USA

Abstract

Two distinct types of microscopic diffusion anisotropy (MA) are compared in brain for both normal control and transgenic (3xTg-AD) mice that develop Alzheimer's disease pathology. The first type of MA is the commonly used microscopic fractional anisotropy (μFA), and the second is a new MA measure referred to as μFA′. These two MA parameters have different symmetry properties that are central to their physical interpretations. Specifically, μFA is invariant with respect to local rotations of compartmental diffusion tensors while μFA′ is invariant with respect to global diffusion tensor deformations. A key distinction between μFA and μFA′ is that μFA is affected by the same type of orientationally coherent diffusion anisotropy as the conventional fractional anisotropy (FA) while μFA′ is not. Furthermore, μFA can be viewed as having independent contributions from both FA and μFA′, as is quantified by an equation relating all three anisotropies. The normal control and transgenic mice are studied at ages ranging from 2 to 15 months with double diffusion encoding MRI being used to estimate μFA and μFA′. In low FA brain regions, μFA and μFA′ are nearly identical, but they show notable differences when FA is large. In particular, μFA and FA are found to be strongly correlated in the fimbria, but μFA′ and FA are not. In addition, both μFA and μFA′ are seen to increase with age in the corpus callosum and external capsule, and modest differences between normal control and transgenic mice are observed for μFA and μFA′ in the corpus callosum and for μFA in the fimbria. The triad of FA, μFA, and μFA′ is proposed as a useful combination of parameters for assessing diffusion anisotropy in brain.

Graphical Abstract

[*]Corresponding author at: Department of Neuroscience, Medical University of South Carolina, Basic Science Building, MSC 510, 173 Ashley Avenue, Suite 403, Charleston, SC, 29425, jense@musc.edu.

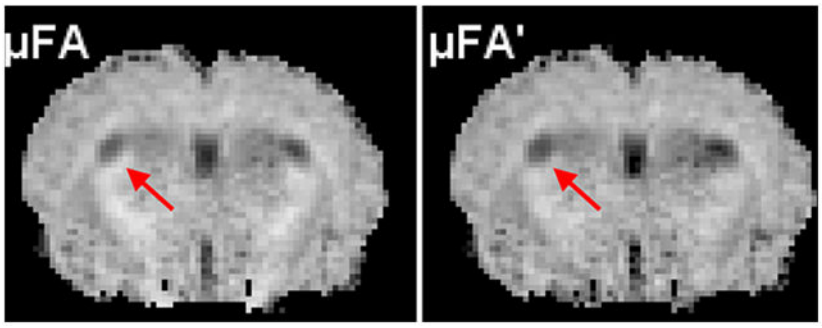

Two different types of microscopic diffusion anisotropy may be defined and quantified with double diffusion encoding MRI. These are investigated in brain for both normal mice and transgenic mice that develop Alzheimer's disease pathology. The metrics for the two types of anisotropy (μFA and μFA′) are characterized by distinct symmetry properties that are reflected in the metrics' experimental values, particularly in white matter regions.

Keywords

microscopic anisotropy; fractional anisotropy; double diffusion encoding MRI; mouse brain; 3xTg-AD; Alzheimer's disease

1 | INTRODUCTION

Diffusion anisotropy is prominent in brain tissue largely because water diffusion is restricted by elongated cytoarchitectural structures such as axons and dendrites.[1] It is most commonly quantified by the diffusion MRI (dMRI) measure of fractional anisotropy (FA), which can be calculated from the diffusion tensor.[2,3] However, the FA is insensitive to diffusion anisotropy when the microstructural elements lack orientational coherence over the length scale set by the imaging voxel dimensions.[4,5] For example, the FA in gray matter is often found to be low despite strong diffusion anisotropy on the microscopic length scale of individual cells.

Diffusion anisotropy that incorporates information from scales comparable to the diffusion length for the dMRI experiment (typically 5–20 μm) regardless of macroscopic orientation coherence is referred to as microscopic diffusion anisotropy or simply microscopic anisotropy (MA).[4–7] There are at least two different conceptions of this.[8] Type-I MA reflects diffusion anisotropy arising from both orientationally coherent and incoherent diffusion restrictions. Thus any diffusive media with a nonzero FA would also have a nonzero type-I MA. Alternatively, one can define type-II MA as diffusion anisotropy that is purely a consequence of incoherent diffusion restrictions so that type-II MA can vanish even if the FA is nonzero.

The above descriptions of type-I and II MA are imprecise, but one can define quantitative diffusion measures that instantiate these concepts. The purpose of this paper is to compare a type-I MA measure known as the microscopic FA (μFA) with a type-II MA measure that we refer to as μFA′. We do this in vivo using both a transgenic (TG) mouse model of Alzheimer's disease (AD) and normal control (NC) mice over an age range of 2 to

15 months. The TG mouse model (3xTg-AD) mimics AD pathology in developing both beta-amyloid plaques and neurofibrillary tangles.[9] Figure 1 gives a schematic that illustrates the qualitative distinctions between FA, μFA, and μFA′.

In order to estimate μFA and μFA′, we apply a double diffusion encoding (DDE)[10] MRI method known as double-pulsed diffusional kurtosis imaging (DP-DKI).[8,11,12] The study of MA has been one of the main applications of DDE MRI,[10] and DP-DKI is a specific version based on an extension of the formalism of conventional (i.e., single diffusion encoding) diffusional kurtosis imaging.[13,14]

2 | METHODS

2.1 | Definition of μFA and μFA′

In order to precisely define quantitative metrics of MA, it is necessary to idealize diffusing water molecules as being restricted to non-exchanging compartments or pores. In brain, these can be identified with the intracellular and extracellular spaces, but it should be kept in mind that water exchange may be important for some dMRI experiments depending on the details of the signal acquisition and brain region. In practice, estimated MA values largely reflect diffusion anisotropy of compartments in which the exchange times are long in comparison to the diffusion and mixing times for the dMRI sequence employed.

Since the compartments are taken to be non-exchanging, each has a well-defined diffusion tensor with three eigenvalues. The μFA is calculated from the average variance of compartmental eigenvalues, $\delta^2\lambda_c$, according to[4,5,7,8]

$$\mu\mathrm{FA} \equiv \sqrt{\frac{3}{2}}\left(1+\frac{\overline{D}^2}{\delta^2\lambda_c}\right)^{-\frac{1}{2}}, \tag{1}$$

where $\overline{D}$ is the mean diffusivity for the full ensemble of compartments. This formula is motivated by an analogous one for the FA in terms of the variance of the eigenvalues, $\delta^2\lambda$, for the total diffusion tensor, namely

$$\mathrm{FA} = \sqrt{\frac{3}{2}}\left(1+\frac{\overline{D}^2}{\delta^2\lambda}\right)^{-\frac{1}{2}}, \tag{2}$$

which can be verified from the usual definition of FA in terms of diffusion tensor eigenvalues.[3] One may also prove the inequality $0 \le \mathrm{FA} \le \mu\mathrm{FA} \le \sqrt{3/2}$, which holds in addition to the standard FA inequality of $0 \le \mathrm{FA} \le 1$.

Here we introduce the type-II MA measure defined by

$$\mu\mathrm{FA}' \equiv \sqrt{\frac{3}{2}}\left(1+\frac{\overline{D}^2}{\delta^2\lambda_c-\delta^2\lambda}\right)^{-\frac{1}{2}}, \tag{3}$$

so that μFA′ = 0 when $\delta^2\lambda_c = \delta^2\lambda$. In addition, it follows directly from Equations 1 and 3 that $0 \le \mu\mathrm{FA}' \le \mu\mathrm{FA}$. From Equations 1–3, one may further show that

$$\frac{\mu\mathrm{FA}^2}{3-2\mu\mathrm{FA}^2} = \frac{\mathrm{FA}^2}{3-2\mathrm{FA}^2} + \frac{\mu\mathrm{FA}'^2}{3-2\mu\mathrm{FA}'^2}. \tag{4}$$

This is reminiscent of the standard formula R2* = R2 + R2′ that relates transverse relaxation rates,[15,16] albeit with more complicated functional forms. Equation 4 implies that any of these three anisotropies can be calculated from the other two. It also shows that if FA > μFA′ then macroscopic anisotropy contributes more to μFA than type-II MA.

An important property of μFA′ is that it is invariant under the transformation

$$\mathbf{D}^{(m)} \to \mathbf{D}^{(m)} + \mathbf{A} - \frac{1}{3}\mathrm{tr}(\mathbf{A})\mathbf{I}, \tag{5}$$

where $\mathbf{D}^{(m)}$ is the diffusion tensor for the mth compartment, **A** is an arbitrary, symmetric "deformation" tensor, and **I** is the identity tensor. This means that a global deformation of the compartmental diffusion tensors does not affect μFA′ even though it does alter both FA and μFA. In this way, μFA′ is specifically sensitive to diffusion anisotropy that is not orientationally coherent, as required for type-II MA. A proof that μFA′ has this symmetry property is sketched in Appendix A. (N.B., some choices of **A** may result in a deformed diffusion tensor having unphysical negative eigenvalues. In such cases, the transformation of Equation 5 should be understood in purely mathematical terms.)

Although μFA is not invariant with respect to the transformation of Equation 5, it is invariant with respect to independent (local) rotations of the compartmental diffusion tensors, which neither FA nor μFA′ is. These two symmetries—global deformation invariance and local rotation invariance—serve to characterize μFA′ and μFA, respectively, and are central to their physical interpretations. Figure 2 demonstrates the two symmetries for a simple example with three compartments. The three anisotropy measures of FA, μFA, and μFA′ are also all invariant with respect to global rotations since they are constructed solely from scalar quantities and thus independent of orientation.

The orientational order parameter (OP)[4,5,17] and anisotropic kurtosis (K_{aniso}),[18,19] which are both used to describe diffusion anisotropy, are related to μFA′ and μFA by

$$\frac{\mu\mathrm{FA}'^2}{3-2\mu\mathrm{FA}'^2} = \left(1-\mathrm{OP}^2\right)\frac{\mu\mathrm{FA}^2}{3-2\mu\mathrm{FA}^2} = \frac{5}{12}\left(1-\mathrm{OP}^2\right)K_{aniso}. \tag{6}$$

Thus, μFA′ = 0 when OP = 1, and μFA′ = μFA when OP = 0. A consequence of Equation 6 is that OP is a measure of neither a type-I nor type-II MA since it lacks the required symmetry properties. However, K_{aniso} is a proper type-I MA parameter with an information content identical to μFA.

2.2 | DP-DKI

DDE MRI sequences have two diffusion encoding time intervals.[10] During each interval, the movement of a given water molecule can be described by a three-dimensional (3D) displacement vector. Let us call these $\mathbf{s}_1$ and $\mathbf{s}_2$. A basic idea behind DP-DKI is that these two 3D vectors can be conveniently concatenated into a single six-dimensional (6D) displacement vector $\tilde{\mathbf{s}} \equiv (\mathbf{s}_1, \mathbf{s}_2)$, where we use a tilde to signify a 6D quantity.[8,11,12,20] The distribution of displacements for the ensemble of diffusion molecules is then fully described by a single 6D probability density function. Associated with this 6D probability density function are a 6D diffusion tensor $\widetilde{\mathbf{D}}$ and a 6D kurtosis tensor $\widetilde{\mathbf{W}}$, which are defined in analogy with the usual 3D case that applies to single diffusion encoding. These two tensors encapsulate all of the DDE MRI information available to second order in the b-value. They can be estimated from DDE MRI data using fitting algorithms that are direct extensions of conventional DKI methods except with more parameters to calculate since the 6D tensors have more components. It should be noted that the conventional 3D diffusion tensor **D** and kurtosis tensor **W** can be extracted as subtensors from $\widetilde{\mathbf{D}}$ and $\widetilde{\mathbf{W}}$. The relationship between the 6D approach used here and an equivalent 3D formalism of Jespersen[21] is described in Ref. 11.

For the purposes of this paper, we only need to consider three scalar measures that are derivable from $\widetilde{\mathbf{D}}$ and $\widetilde{\mathbf{W}}$. The first is the mean of 3D kurtosis tensor given by[22,23]

$$\overline{W} = \frac{1}{5}(W_{1111} + W_{2222} + W_{3333} + 2W_{1122} + 2W_{1133} + 2W_{2233}), \tag{7}$$

where W_{ijkl} is a component of **W.** The second is the mean of the 6D kurtosis tensor given by[8,11,12,20]

$$\begin{aligned}\overline{\widetilde{W}} = \frac{1}{8}\big(&\widetilde{W}_{1111} + \widetilde{W}_{2222} + \widetilde{W}_{3333} + 2\widetilde{W}_{1122} + 2\widetilde{W}_{1133} + 2\widetilde{W}_{2233} \\ &+ \widetilde{W}_{1144} + \widetilde{W}_{2255} + \widetilde{W}_{3366} + 2\widetilde{W}_{1155} + 2\widetilde{W}_{1166} + 2\widetilde{W}_{2266}\big),\end{aligned} \tag{8}$$

$\widetilde{W}_{\alpha\beta\gamma\delta}$ is a component of $\widetilde{\mathbf{W}}$. Finally, we use the conventional FA, which is determined from **D** according to Equation 2.

While both $\overline{W}$ and $\overline{\widetilde{W}}$ are generally valid measures of diffusional kurtosis, they can be explicitly related to the compartmental diffusion tensor eigenvalues for the special case that the diffusive media consists of non-exchanging, Gaussian compartments. Specifically, one can show that the difference between the 3D and 6D mean kurtosis is[8]

$$\delta\overline{W} \equiv \overline{W} - \overline{\widetilde{W}} = \frac{9}{20\overline{D}^2}\left(\delta^2\lambda_c - \delta^2\lambda\right). \tag{9}$$

By combining Equations 3 and 9, we then find

$$\mu\mathrm{FA}' \equiv \sqrt{\frac{3}{2}}\left(1 + \frac{9}{20\delta\overline{W}}\right)^{-\frac{1}{2}} = \sqrt{\frac{30\delta\overline{W}}{9 + 20\delta\overline{W}}}. \tag{10}$$

Thus, μFA′ can be easily determined from the means of the 3D and 6D kurtosis tensors with the help of Equations 7–10. Given FA and μFA′, one can then find μFA from Equation 4. In prior work, $\delta\overline{W}$ is proposed as an index of type-II MA.[8] Here we have introduced μFA′ since it is more directly analogous to FA and μFA. Nonetheless, as is evident from Equation 10, $\delta\overline{W}$ and μFA′ contain the same information. We emphasize that this relationship between $\delta\overline{W}$ and μFA′ is contingent upon an assumption of non-exchanging, Gaussian compartments, which we adopt in this paper for our data analysis, as have several related studies.[4,5,7,17,24–27] Importantly, however, the definitions of μFA and μFA′, their symmetry properties, and the interrelationship of Equation 4 do not require the compartments to be Gaussian.

While non-exchanging, Gaussian compartments are assumed for a variety of other dMRI approaches,[28–30] many of these include additional assumptions, such as a specific number of compartments and detailed constraints on their compartmental diffusion tensors, which in some cases have been controversial.[31,32] Thus, the presuppositional weight of the approach followed here is relatively modest. Nonetheless, diffusion restrictions, as found in the brain, do typically result in some degree of intracompartmental non-Gaussianity,[18,19] which may impact the accuracy of estimates for μFA′ obtained from Equation 10.

2.3 | Animals

Our experiments used 32 TG and 25 NC female mice with ages ranging from 2 to 15 months, and they were performed under a protocol approved by the Institutional Animal Care and Use Committee of the Medical University of South Carolina. All mice were obtained from The Jackson Laboratory (Bar Harbor, ME, USA) and housed in climate-controlled rooms on a 12-hr light/dark cycle in an accredited animal care facility. The TG mouse model was 3xTg-AD [B6;129-Psen1tm1Mpm Tg(APPSwe,tauP301L) 1Lfa/Mmjax; MMRRC Stock No: 34830-JAX|3xTg-AD]. This model develops both beta-amyloid plaques and neurofibrillary tangles in brain as the mice age, and it is a widely used to investigate AD pathology.[9,33] The NC mice (101,045 B6129SF2/J) were recommended controls for the TG mice. We selected only females since male 3xTg-AD mice do not consistently develop AD pathology.[34,35]

2.4 | Imaging

For scanning with MRI, mice were anesthetized using an isoflurane vaporizer set at 3% for induction and 2% for data acquisition. Both respiration and rectal temperature were recorded with an animal monitoring unit (SA instruments, Inc., model 1025, Stony Brook, NY), and body temperature was maintained using ventilated warm air. To minimize motion artifacts, mice were restrained with tooth and ear bars. During the scans, body temperature was stable at 37.0 ± 0.2 °C, and respiration ranged between 60 and 80 breaths per minute.

All mice were scanned in vivo on a Bruker 7T BioSpec 70/30 MRI system (Billerica, MA, USA) having a maximum gradient amplitude of 440 mT/m and running ParaVision 5.1 software. A four-channel head coil was employed for signal reception. Imaging data were acquired using a previously described, custom DDE MRI pulse sequence with a two-shot echo planar readout and partial Fourier acceleration of 1.5.[11] The main image parameters

were: TR = 3000 ms, TE = 51.3 ms, diffusion time = 11 ms, pulse duration = 5.3 ms, mixing time = 20.8 ms, acquisition matrix = 128×128, number of slices = 6 (no gap), FOV = 20×20 mm^2, slice thickness = 0.7 mm, in-plane resolution = 0.156×0.156 mm^2, 80 (6D) diffusion encoding directions, 6 nonzero *b*-values for each diffusion encoding direction (500, 1000, 1500, 2000, 2500, and 3000 s/mm^2), 2 repetitions, and 10 acquisitions with the *b*-value set to 0. The total acquisition time for this sequence was 98 minutes. The 6D diffusion encoding directions were optimized for DP-DKI as described in previous work.[12] An advantage of using DDE MRI with short pulse durations, compared to alternative magic angle spinning of the q-vector methods,[17,36] is relative insensitivity to any diffusion tensor time dependence.[37]

Coronal DDE MRI images were obtained for each mouse at a single time point between 2 and 15 months of age. Images from 1 TG mouse and 2 NC mice were excluded from the data analysis due to excessive ghosting artifacts. Of the remaining mice, 8 TG and 6 NC mice were scanned at 2 months, 8 TG and 6 NC mice were scanned at 5 months, 5 TG and 4 NC mice were scanned at 8 months, 5 TG and 5 NC mice were scanned at 12 months, and 5 TG and 2 NC mice were scanned at 15 months. Direction-averaged DDE MRI images for one mouse are provided in the Supporting Information (Figure S1).

2.5 | Data processing

Preprocessing of the DDE MRI data included denoising,[38] motion correction, Gaussian smoothing with a kernel of 1.25 times the voxel dimensions, and rectified noise bias correction. The noise bias correction was based on the standard method proposed by McGibney and Smith[39] and by Miller and Joseph[40] generalized to multiple channel coils, as described in Appendix B. The 6D diffusion and kurtosis tensors were obtained using in house software that implemented the method of Shaw and coworkers,[12] which employs a constrained weighted least squares fitting algorithm similar to ones routinely used for DKI.[41,42]

Parametric maps of μFA′ were then constructed by applying Equations 7–10. The 3D diffusion tensor was extracted as a subtensor from the 6D diffusion tensor and used to calculate the FA maps. Finally, μFA maps were determined from the formula

$$\mu\mathrm{FA} = \sqrt{3 \cdot \frac{3\mathrm{FA}^2 + 3\mu\mathrm{FA}'^2 - 4\mathrm{FA}^2\mu\mathrm{FA}'^2}{9 - 4\mathrm{FA}^2\mu\mathrm{FA}'^2}}. \tag{11}$$

which follows from Equation 4. The corresponding formula for calculating μFA′ from FA and μFA is

$$\mu\mathrm{FA}' = 3\sqrt{\frac{\mu\mathrm{FA}^2 - \mathrm{FA}^2}{9 - 12\mathrm{FA}^2 + 4\mathrm{FA}^2\mu\mathrm{FA}^2}}. \tag{12}$$

While Equation 12 was not needed in our data analysis, it may be useful in conjunction with other dMRI approaches[4,5,7,17,24–26,43,44] that estimate μFA more directly and is given here for the sake of completeness.

A region of interest (ROI) analysis was used to compare the three anisotropies within the fimbria (Fi), corpus callosum (CC), external capsule (EC), dorsal hippocampus (DH), and ventral hippocampus (VH). For these five brain regions, all ROIs were drawn manually on FA maps by a single individual (JV), guided by comparison with a standard mouse atlas,[45] and confirmed by an experienced neuropathologist (MFF). The analysis was not blinded with respect to age or mouse type. Example ROIs are shown in Figure 2. The ROIs for the Fi, CC, EC, DH, and VH contained voxels from 3, 5, 5, 2 and 2 imaging slices, respectively, and voxels from the left and right sides of the brain were pooled. The Fi, CC, and EC are considered to be white matter while the DH and VH are considered to be gray matter. The regional values for dMRI measures were obtained by averaging all voxels within an ROI except for those with $\overline{D} > 1.5\ \mu m^2/ms$, which were excluded to reduce partial volume effects due to cerebrospinal fluid. Correlations between parameters were assessed with coefficients of determination (R^2) for linear least squares fits to the data. Group comparisons used a two-tailed t-test assuming unequal variances.

3 | RESULTS

Representative FA, μFA, and μFA′ maps are given in Figure 4 for a single coronal brain slice of an NC mouse (top row) and a TG mouse (bottom row). Observe that μFA is larger than both FA and μFA′ throughout the brain since it incorporates contributions from each, as suggested by Equation 4. In low FA regions, μFA and μFA′ are nearly the same. However, in high FA regions, μFA is noticeably larger than μFA′. This can be seen, for example, in Fi (red arrows) as well as in other white matter regions. The relative elevation in μFA reflects the impact of macroscopic anisotropy, which is absent from μFA′.

Figure 5 plots the values of FA, μFA, and μFA′ for all five brain regions considered at all five ages from all 54 mice that had acceptable quality DDE MRI images. Also shown are best fit linear regression lines along with coefficients of determination and p-values. Solid lines are used for significant correlations ($p < 0.05$) while dotted lines are used otherwise. Significant correlations are seen for all three anisotropies in CC and EC as well as for FA in DH. In all of these cases, the slopes of the regression lines are positive reflecting an increase in anisotropy with age. However, the correlations were only moderate in strength with the highest coefficient of determination being $R^2 = 0.26$ for the μFA in CC. In calculating these correlations, the two groups were pooled for the sake of simplicity. However, in the cases that significant correlations were found for the pooled data, the individual group correlations with age were also statistically significant with the exceptions of the μFA and μFA′ correlations in EC for NC mice.

The correlations between the three anisotropies for all five brain regions are given in Figure 6. The μFA and μFA′ are strongly correlated in all regions. In EC, DH, and VH, the R^2 values were 0.99 showing that these two anisotropies have virtually identical information content. However, for Fi and CC, the correlations are substantially lower ($R^2 = 0.66$ and 0.85). The μFA is also strongly correlated with FA in the three white matter regions ($R^2 =$ 0.47, 0.54, and 0.55). While μFA′ is strongly correlated with FA in EC ($R^2 = 0.45$), it is only moderately correlated with FA in CC ($R^2 = 0.17$) and not significantly correlated with FA in

Fi. This contrast in the correlations with FA for the two types of MA reflects the fact that μFA includes contributions from macroscopic anisotropy while μFA′ does not.

A comparison of the anisotropies for NC and TG mice is provided in Figure 7, with the data from all five time points being pooled together. The values for the NC and TG mice are similar, but significant differences are found in a few cases. Specifically, group differences for FA and μFA are found in Fi ($p = 0.035$ and 0.009), for μFA and μFA′ in CC ($p = 0.040$ and 0.045), and for FA in both DH and VH ($p = 0.016$ and $p < 10^{-4}$). These p-values have not been corrected for multiple comparisons, but the FA difference in VH would survive a Bonferroni correction with 15 comparisons. Inspection of Figure 5(m) suggests that this difference for VH is driven primarily by the data at ages 5 and 8 months, which is early relative to the development of AD pathology in the TG mouse model[9,27] but broadly consistent with histological observations of hippocampal myelin abnormalities for 3xTg-AD mice at 2 and 6 months.[46]

4 | DISCUSSION

A primary advantage of DDE MRI over conventional single diffusion encoding dMRI is its sensitivity to MA.[10] A commonly used measure for MA is μFA, as defined by Equation 1.[4,5,7,17,24–26,43,44] The μFA is characterized by invariance with respect to local rotations of compartmental diffusion tensors—a symmetry not shared by FA. Here we have proposed μFA′ as a new MA measure defined by Equation 3. The characteristic symmetry for μFA′ is invariance with respect to global deformations in the compartmental diffusion tensors of the form given by Equation 5. The μFA, in contrast, does not possess global deformation invariance, but it is worth noting that the minimum μFA over all possible global deformations is precisely μFA′. In this sense, μFA′ can be viewed as the residual part of μFA after its macroscopic component has been removed. These two MA measures are specific examples the type-I and type-II MA as discussed above and elsewhere.[8]

An explicit relationship between FA, μFA, and μFA′ is provided by Equation 4. This shows that given any two of these three quantities the third can be calculated. The three anisotropies thus form a triad similar to R2, R2*, and R2′. Each of these three transverse relaxivities provides complementary information,[16] and we have argued that the same holds true for FA, μFA, and μFA′. In particular, as expressed by Equation 4, μFA can be regarded as having contributions from FA (macroscopic anisotropy) and μFA′ (type-II MA). Thus knowledge of μFA′ can inform the physical interpretation of μFA. For example, if FA $\gg$ μFA′, then μFA would reflect mostly anisotropy that is orientationally coherent. The μFA′ may be of particular interest in brain regions, such as the corpus striatum, that consist of multiple components with differing degrees of orientational coherence. Here it could help determine whether group differences observed for FA and μFA are associated mainly with coherent structures (e.g., myelinated fiber bundles) or also involve a more orientationally disordered component (e.g., unmyelinated neurites). Formulae for obtaining either μFA or μFA′ from the other two anisotropies are given by Equations 11 and 12.

For mouse brain, we find μFA and μFA′ to be similar in the brain regions investigated, but they show important differences in their correlations with FA. Most notably, μFA and FA

are highly correlated in Fi while μFA′ and FA are not. This reflects a strong contribution to μFA from macroscopic anisotropy that is absent for μFA′. Our mouse brain results also show that both μFA and μFA′ increase with age in CC and EC, suggesting these parameters may be useful in tracking age-related microstructural changes. In addition, we find modest differences between NC and TG mice for both μFA and μFA′ in CC and for μFA in Fi, but these should be interpreted with caution considering the wide range in ages (2–15 months) and the relatively small number of animals assessed at each time point.

We also observe a significant increase in FA with age in the CC, EC, and DH. This is in contrast with two prior dMRI studies of 3xTg-AD mice which did not find significant changes in FA with age.[47,48] However, the age for the first time point (2 months) in our study is substantially younger than that of the two prior studies (11 months[47] and 4.5 months[48]). Indeed, when this first time point is excluded from our analysis, we no longer obtain significant correlations between FA and age.

As suggested by Figures 4–7, the apparent precisions of μFA and μFA′ estimates are similar for our experiment. However, this observation may not to generalize to other DDE MRI approaches that employ different methods. An in-depth study of the precision and accuracy for DDE MRI measurement of μFA is given by Kerkelä and coworkers.[49]

There are three important limitations to this study. First, the definitions of both μFA and μFA′ assume distinct microstructural compartments. Because intercompartmental water exchange can be significant in brain,[50] the estimated values of these two parameters may depend somewhat on the diffusion and mixing times of the DDE MRI pulse sequence, which affect the extent to which water molecules stay within a single compartment during the signal acquisition. Second, although not necessary for their definitions, our method for measuring μFA and μFA′ also assumes Gaussian diffusion within each compartment. While many brain tissue microstructural models share this assumption,[4,5,7,17,24–30,51] there is recent evidence of a small intracompartmental kurtosis in healthy brain[12,18,52] and more substantial values for ischemic stroke.[53] Third, the image acquisition time (98 min) for our experiment is rather long. However, that is due to the use of 80 6D diffusion encoding directions and 6 nonzero b-values. This large number of diffusion encoding directions was chosen in order to determine the full 6D diffusion and kurtosis tensors, which requires a minimum of 66 directions.[12] As discussed in prior work,[8,11] sufficient data can be acquired for estimation of FA and $\delta\overline{W}$ (and hence μFA and μFA′) from just 21 directions and 2 nonzero b-values. Therefore, substantially shorter image acquisitions should be possible with our approach. In addition, other established methods for estimating μFA[4,5,7,17,24–27,43,44] could be easily extended to also determine μFA′ (e.g., by using Equation 12).

5 | CONCLUSION

We have provided a direct comparison of two different types of MA in brain for both NC and 3xTg-AD mice, which exhibit the major hallmarks of AD pathology, over a wide range of ages. In particular, we have considered the commonly used μFA along with the new MA measure of μFA′. Each of these parameters instantiates a distinct type of

MA, and they are characterized by different symmetry properties. We argue that μFA′, in contrast to μFA, is unaffected by the macroscopic anisotropy captured by FA and may therefore be more specific to MA arising from orientationally incoherent microstructural elements. Nonetheless, μFA′ can be easily calculated from FA and μFA, and it is therefore straightforward to incorporate as part of the data analysis for any of a variety of dMRI methods suitable for quantifying MA. The three diffusion anisotropies of FA, μFA, and μFA′ provide complementary information, and their use in combination may help in characterizing brain microstructure. For the NC and TG mice studied here, we find both μFA, and μFA′ to increase with age in some white matter regions along with evidence for modest group differences in these two anisotropy measures.

Supplementary Material

Refer to Web version on PubMed Central for supplementary material.

ACKNOWLEDGMENTS

This work was supported, in part, by the National Institutes of Health (RF1AG057602 and R01AG054159) and by the Litwin Foundation.

APPENDIX A: Invariance of μFA′ under global diffusion tensor deformations

The global deformation of Equation 5 adds an arbitrary, symmetric traceless tensor (i.e., $\mathbf{A} - \mathrm{tr}(\mathbf{A})\mathbf{I}/3$) to all of the compartmental diffusion tensors and, consequently, to the total diffusion tensor $\mathbf{D}$ as well. Since the mean diffusivity for the mth compartment is

$$\bar{D}^{(m)} = \frac{1}{3}\mathrm{tr}\left(\mathbf{D}^{(m)}\right), \tag{A1}$$

the compartmental diffusivities are unchanged by this transformation. This also holds for the total diffusivity, which can be written as

$$\bar{D} = \sum_{m=1}^{N} f_m \bar{D}^{(m)}, \tag{A2}$$

where N is the total number of compartments and f_m is the water fraction for each compartment (assumed to sum up to one). However, it is not true for the variance of eigenvalues as can be seen from the expression

$$\delta^2\lambda = \frac{1}{3}\mathrm{tr}\left[\left(\mathbf{D} - \bar{D}\mathbf{I}\right)^2\right] \tag{A3}$$

or for the corresponding expression for the average variance of compartmental eigenvalues

$$\delta^2\lambda_c = \frac{1}{3}\sum_{m=1}^{N} f_m \,\mathrm{tr}\left[\left(\mathbf{D}^{(m)} - \bar{D}^{(m)}\mathbf{I}\right)^2\right]. \tag{A4}$$

Nevertheless, the difference between these two variances does not change under the transformation of Equation 5. This is evident from

$$\delta^2\lambda_c - \delta^2\lambda = \frac{1}{3}\sum_{m=1}^{N} f_m \,\mathrm{tr}\left[\left(\mathbf{D}^{(m)} - \bar{D}^{(m)}\mathbf{I} - \mathbf{D} + \bar{D}\mathbf{I}\right)^2\right], \tag{A5}$$

because the shift in $\mathbf{D}^{(m)}$ is canceled by the shift in **D.** Equation A5 may be verified by using Equations A2–A4, the expression $\mathbf{D} = \sum_{m=1}^{N} f_m \mathbf{D}^{(m)}$, and linearity of the trace operation. Finally, since the definition of Equation 3 for μFA′ depends only on $\bar{D}$ and $\delta^2\lambda_c - \delta^2\lambda$, μFA′ must also be invariant.

APPENDIX B: Correction for noise bias

To reduce signal bias due to rectified noise in MRI magnitude images, a commonly used formula is

$$S = \sqrt{M^2 - 2\sigma^2} \tag{B1}$$

where S is the corrected signal, M is the measured signal, and σ is the signal noise.[39,40] However, this approach is only valid for Rician noise. In our experiment, we acquired DDE MRI data using a four-channel phased array head coil with a sum-of-squares signal reconstruction. As a consequence, the noise follows a noncentral chi distribution, and Equation B1 is generalized to

$$S = \sqrt{M^2 - 2n\sigma^2}, \tag{B2}$$

where n is the number of coils and with noise correlations between the coil channels being neglected.[54–56] The noise can be estimated from the background (air) signal, M_0, according to[55]

$$\sigma = \frac{\Gamma(n)M_0}{\sqrt{2}\Gamma\left(n+\frac{1}{2}\right)}. \tag{B3}$$

Since we employed a four-channel coil, we set $n = 4$ to find

$$\sigma = \frac{32M_0}{35\sqrt{2\pi}} \approx 0.365M_0, \tag{B4}$$

and corrected our DDE MRI data according to Equation B2, with the corrected signal being set to zero whenever the argument of the square root was negative.

Abbreviations used:

AD	Alzheimer’s disease
CC	corpus callosum

DH	dorsal hippocampus
dMRI	diffusion MRI
DDE MRI	double diffusion encoding MRI
DP-DKI	double-pulsed diffusional kurtosis imaging
EC	external capsule
FA	fractional anisotropy
Fi	fimbria
MA	microscopic anisotropy
μFA	type-I microscopic fractional anisotropy
μFA′	type-II microscopic fractional anisotropy
NC	normal control
OP	order parameter
ROI	region of interest
TG	transgenic
VH	ventral hippocampus
3D	three dimensional
6D	six dimensiona

REFERENCES

1. Beaulieu C The basis of anisotropic water diffusion in the nervous system–a technical review. NMR Biomed. 2002;15:435–455. [PubMed: 12489094]
2. Basser PJ, Pierpaoli C. Microstructural and physiological features of tissues elucidated by quantitative-diffusion-tensor MRI. J Magn Reson. 2011;213:560–570. [PubMed: 22152371]
3. Westin CF, Maier SE, Mamata H, Nabavi A, Jolesz FA, Kikinis R. Processing and visualization for diffusion tensor MRI. Med Image Anal. 2002;6:93–108. [PubMed: 12044998]
4. Lasič S, Szczepankiewicz F, Eriksson S, Nilsson M, Topgaard D. Microanisotropy imaging: quantification of microscopic diffusion anisotropy and orientational order parameter by diffusion MRI with magic-angle spinning of the q-vector. Front Phys. 2014;2:11.
5. Szczepankiewicz F, Lasič S, van Westen D, et al. Quantification of microscopic diffusion anisotropy disentangles effects of orientation dispersion from microstructure: applications in healthy volunteers and in brain tumors. NeuroImage. 2015;104:241–252. [PubMed: 25284306]
6. Lawrenz M, Koch MA, Finsterbusch J. A tensor model and measures of microscopic anisotropy for double-wave-vector diffusion-weighting experiments with long mixing times. J Magn Reson. 2010;202:43–56. [PubMed: 19854085]
7. Henriques RN, Jespersen SN, Shemesh N. Microscopic anisotropy misestimation in spherical-mean single diffusion encoding MRI. Magn Reson Med. 2019;81:3245–3261. [PubMed: 30648753]
8. Hui ES, Jensen JH. Double-pulsed diffusional kurtosis imaging for the in vivo assessment of human brain microstructure. NeuroImage. 2015;120:371–381. [PubMed: 26172309]

9. Oddo S, Caccamo A, Shepherd JD, et al. Triple-transgenic model of Alzheimer's disease with plaques and tangles: intracellular Aβ and synaptic dysfunction. Neuron. 2003;39:409–421. [PubMed: 12895417]
10. Shemesh N, Jespersen SN, Alexander DC, et al. Conventions and nomenclature for double diffusion encoding NMR and MRI. Magn Reson Med. 2016;75:82–87. [PubMed: 26418050]
11. Jensen JH, Hui ES, Helpern JA. Double-pulsed diffusional kurtosis imaging. NMR Biomed. 2014;27:363–370. [PubMed: 24623712]
12. Shaw CB, Hui ES, Helpern JA, Jensen JH. Tensor estimation for double-pulsed diffusional kurtosis imaging. NMR Biomed. 2017;30:e3722.
13. Jensen JH, Helpern JA, Ramani A, Lu H, Kaczynski K. Diffusional kurtosis imaging: the quantification of non-Gaussian water diffusion by means of magnetic resonance imaging. Magn Reson Med. 2005;53:1432–1440. [PubMed: 15906300]
14. Jensen JH, Helpern JA. MRI quantification of non-Gaussian water diffusion by kurtosis analysis. NMR Biomed. 2010;23:698–710. [PubMed: 20632416]
15. Yablonskiy DA, Haacke EM. Theory of NMR signal behavior in magnetically inhomogeneous tissues: the static dephasing regime. Magn Reson Med. 1994;32:749–763. [PubMed: 7869897]
16. Ma J, Wehrli FW. Method for image-based measurement of the reversible and irreversible contribution to the transverse-relaxation rate. J Magn Reson, Series B. 1996;111:61–69.
17. Westin CF, Knutsson H, Pasternak O, Szczepankiewicz F, Özarslan E, van Westen D, Mattisson C, Bogren M, O'Donnell LJ, Kubicki M, Topgaard D. Q-space trajectory imaging for multidimensional diffusion MRI of the human brain. NeuroImage. 2016;135:345–362. [PubMed: 26923372]
18. Henriques RN, Jespersen SN, Shemesh N. Correlation tensor magnetic resonance imaging. NeuroImage. 2020;211:116605.
19. Henriques RN, Jespersen SN, Shemesh N. Evidence for microscopic kurtosis in neural tissue revealed by correlation tensor MRI. Magn Reson Med. 2021;86:3111–3130. [PubMed: 34329509]
20. Jensen JH. Stejskal's formula for multiple-pulsed diffusion MRI. Magn Reson Imaging. 2015;33:1182–1186. [PubMed: 26220858]
21. Jespersen SN. Equivalence of double and single wave vector diffusion contrast at low diffusion weighting. NMR Biomed. 2012;25:813–818. [PubMed: 22134913]
22. Hansen B, Lund TE, Sangill R, Jespersen SN. Experimentally and computationally fast method for estimation of a mean kurtosis. Magn Reson Med. 2013;69:1754–1760. [PubMed: 23589312]
23. Hansen B, Lund TE, Sangill R, Stubbe E, Finsterbusch J, Jespersen SN. Experimental considerations for fast kurtosis imaging. Magn Reson Med. 2016;76:1455–1468. [PubMed: 26608731]
24. Jespersen SN, Lundell H, Sønderby CK, Dyrby TB. Orientationally invariant metrics of apparent compartment eccentricity from double pulsed field gradient diffusion experiments. NMR Biomed. 2013;26:1647–1662. [PubMed: 24038641]
25. Jespersen SN, Lundell H, Sønderby CK, Dyrby TB. Commentary on "Microanisotropy imaging: quantification of microscopic diffusion anisotropy and orientation of order parameter by diffusion MRI with magic-angle spinning of the q-vector". Front Phys. 2014;2:28.
26. Szczepankiewicz F, van Westen D, Englund E, et al. The link between diffusion MRI and tumor heterogeneity: Mapping cell eccentricity and density by diffusional variance decomposition (DIVIDE). NeuroImage. 2016;142:522–532. [PubMed: 27450666]
27. Topgaard D Multidimensional diffusion MRI. J Magn Reson. 2017;275:98–113. [PubMed: 28040623]
28. Yablonskiy DA, Sukstanskii AL. Theoretical models of the diffusion weighted MR signal. NMR Biomed 2010;23:661–681. [PubMed: 20886562]
29. Novikov DS, Fieremans E, Jespersen SN, Kiselev VG. Quantifying brain microstructure with diffusion MRI: Theory and parameter estimation. NMR Biomed. 2019;32:e3998.
30. Jensen JH. Frontiers of microstructural imaging with diffusion MRI. In: Huang H, Roberts TPL (eds.). Advances in Magnetic Resonance Technology and Applications (Vol. 2): Handbook of Pediatric Brain Imaging. Academic Press: London; 2021, Chapter 2.

31. Jelescu IO, Veraart J, Fieremans E, Novikov DS. Degeneracy in model parameter estimation for multi-compartmental diffusion in neuronal tissue. NMR Biomed. 2016;29:33–47. [PubMed: 26615981]
32. Novikov DS, Kiselev VG, Jespersen SN. On modeling. Magn Reson Med. 2018;79:3172–3193. [PubMed: 29493816]
33. Martini AC, Forner S, Trujillo-Estrada L, Baglietto-Vargas D, LaFerla FM. Past to future: what animal models have taught us about Alzheimer's disease. J Alzheimer's Dis. 2018;64(s1):S365–S378. [PubMed: 29504540]
34. Carroll JC, Rosario ER, Kreimer S, et al. Sex differences in β-amyloid accumulation in 3xTg-AD mice: role of neonatal sex steroid hormone exposure. Brain Res. 2010;1366:233–245. [PubMed: 20934413]
35. Belfiore R, Rodin A, Ferreira E, et al. Temporal and regional progression of Alzheimer's disease-like pathology in 3xTg-AD mice. Aging Cell. 2019;18:e12873.
36. Eriksson S, Lasic S, Topgaard D. Isotropic diffusion weighting in PGSE NMR by magic-angle spinning of the q-vector. J Magn Reson. 2013;226:13–18. [PubMed: 23178533]
37. Jespersen SN, Olesen JL, Ianuş A, Shemesh N. Effects of nongaussian diffusion on "isotropic diffusion" measurements: An ex-vivo microimaging and simulation study. J Magn Reson. 2019;300:84–94. [PubMed: 30711786]
38. Veraart J, Novikov DS, Christiaens D, Ades-Aron B, Sijbers J, Fieremans E. Denoising of diffusion MRI using random matrix theory. NeuroImage. 2016;142:394–406. [PubMed: 27523449]
39. McGibney G, Smith MR. An unbiased signal-to-noise ratio measure for magnetic resonance images. Med Phys. 1993;20:1077–1078. [PubMed: 8413015]
40. Miller AJ, Joseph PM. The use of power images to perform quantitative analysis on low SNR MR images. Magn Reson Imaging. 1993;11:1051–1056. [PubMed: 8231670]
41. Tabesh A, Jensen JH, Ardekani BA, Helpern JA. Estimation of tensors and tensor-derived measures in diffusional kurtosis imaging. Magn Reson Med. 2011;65:823–836. [PubMed: 21337412]
42. Veraart J, Sijbers J, Sunaert S, Leemans A, Jeurissen B. Weighted linear least squares estimation of diffusion MRI parameters: strengths, limitations, and pitfalls. NeuroImage. 2013;81:335–346. [PubMed: 23684865]
43. Ianuş A, Jespersen SN, Duarte TS, Alexander DC, Drobnjak I, Shemesh N. Accurate estimation of microscopic diffusion anisotropy and its time dependence in the mouse brain. NeuroImage. 2018;183:934–949. [PubMed: 30145206]
44. Yang G, Tian Q, Leuze C, Wintermark M, McNab JA. Double diffusion encoding MRI for the clinic. Magn Reson Med. 2018;80:507–520. [PubMed: 29266375]
45. Paxinos G, Franklin KBJ. The Mouse Brain in Stereotaxic Coordinates. Compact 2nd ed. San Diego, CA: Elsevier; 2004.
46. Desai MK, Sudol KL, Janelsins MC, Mastrangelo MA, Frazer ME, Bowers WJ. Triple-transgenic Alzheimer's disease mice exhibit region-specific abnormalities in brain myelination patterns prior to appearance of amyloid and tau pathology. Glia. 2009;57:54–65. [PubMed: 18661556]
47. Kastyak-Ibrahim MZ, Di Curzio DL, Buist R, Herrera SL, Albensi BC, Del Bigio MR, Martin M. Neurofibrillary tangles and plaques are not accompanied by white matter pathology in aged triple transgenic-Alzheimer disease mice. Magn Reson Imaging. 2013;31:1515–1521. [PubMed: 23993791]
48. Nie X, Falangola MF, Ward R, McKinnon ET, Helpern JA, Nietert PJ, Jensen JH. Diffusion MRI detects longitudinal white matter changes in the 3xTg-AD mouse model of Alzheimer's disease. Magn Reson Imaging. 2019;57:235–242. [PubMed: 30543850]
49. Kerkelä L, Henriques RN, Hall MG, Clark CA, Shemesh N. Validation and noise robustness assessment of microscopic anisotropy estimation with clinically feasible double diffusion encoding MRI. Magn Reson Med. 2020;83:1698–1710. [PubMed: 31651995]
50. Nilsson M, van Westen D, Ståhlberg F, Sundgren PC, Lätt J. The role of tissue microstructure and water exchange in biophysical modelling of diffusion in white matter. Magn Reson Mater Phy. 2013;26:345–370.

51. Panagiotaki E, Schneider T, Siow B, Hall MG, Lythgoe MF, Alexander DC. Compartment models of the diffusion MR signal in brain white matter: a taxonomy and comparison. NeuroImage. 2012;59:2241–2254. [PubMed: 22001791]

52. Novello L, Henriques RN, Ianuş A, Feiweier T, Shemesh N, Jovicich J. In vivo correlation tensor MRI reveals microscopic kurtosis in the human brain on a clinical 3T scanner. NeuroImage. 2022:119137.

53. Alves R, Henriques RN, Kerkelä L, Chavarrías C, Jespersen SN, Shemesh N. Correlation tensor MRI deciphers underlying kurtosis sources in stroke. NeuroImage. 2022;247:118833.

54. Constantinides CD, Atalar E, McVeigh ER. Signal-to-noise measurements in magnitude images from NMR phased arrays. Magn Reson Med. 1997;38:852–857. [PubMed: 9358462]

55. Aja-Fernández S, Tristán-Vega A, Alberola-López C. Noise estimation in single-and multiple-coil magnetic resonance data based on statistical models. Magn Reson Imaging. 2009;27:1397–1409. [PubMed: 19570640]

56. Aja-Fernández S, Brion V, Tristán-Vega A. Effective noise estimation and filtering from correlated multiple-coil MR data. Magn Reson Imaging. 2013;31:272–285. [PubMed: 23122024]

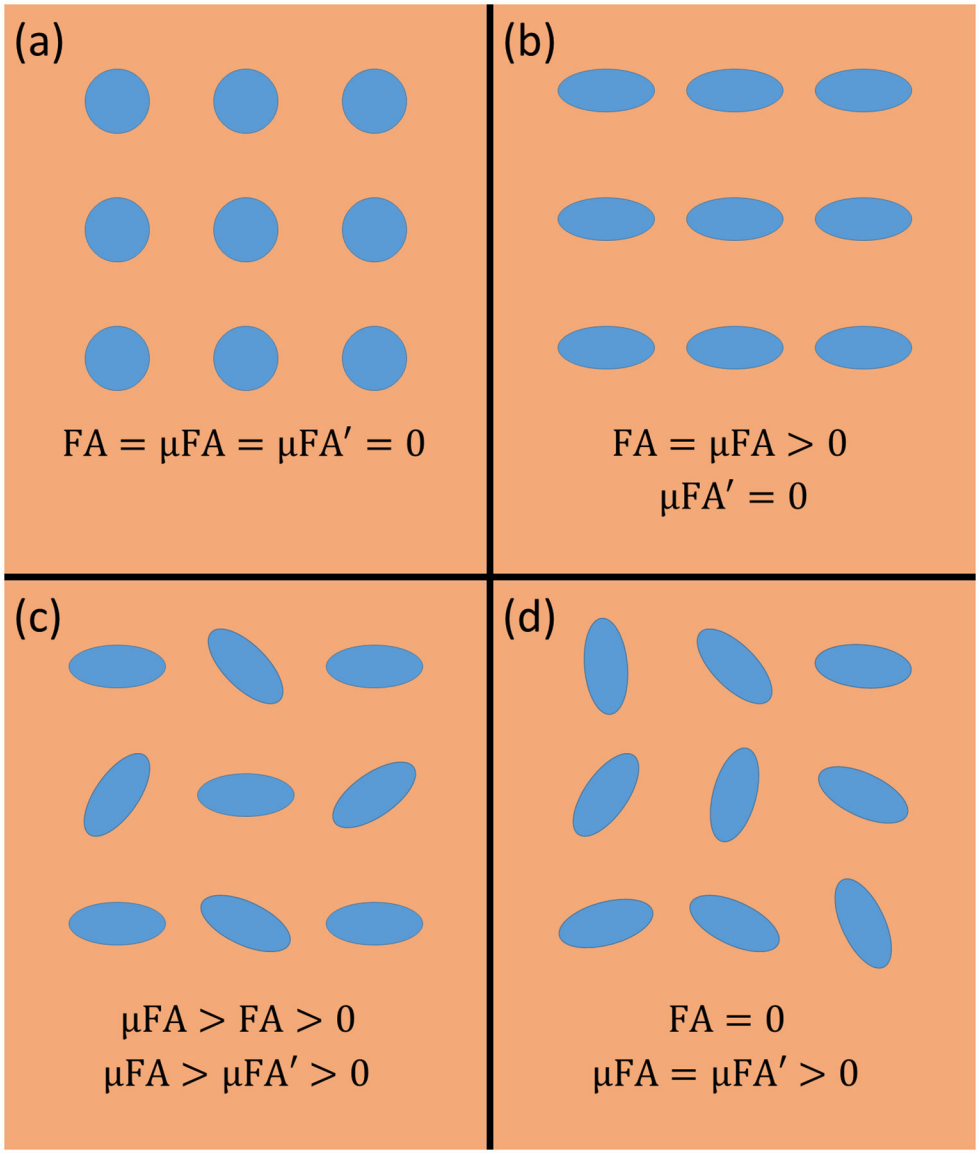

FIGURE 1:

Schematics of water confined to ellipsoidal pores (blue) illustrating the two types of microscopic anisotropy (MA) along with the macroscopic anisotropy associated with orientationally coherent microstructural compartments. The fractional anisotropy (FA) is a conventional measure of macroscopic anisotropy while μFA quantifies type-I MA and μFA′ quantifies type-II MA. (a) Spherical pores have no preferred direction, and all three anisotropies therefore vanish. (b) Elongated pores that are all identical with the same orientation have positive FA and μFA, but μFA′ still vanishes since it is only sensitive to MA that is distinct from the macroscopic anisotropy captured by FA. (c) FA, μFA and μFA′ are all positive for elongated pores with some microscopic disorder in orientations but still a net preferred direction (horizontal in this case), and μFA is larger than either FA or μFA′. (d) Elongated pores with random orientations have zero FA while μFA and μFA′ are positive and equal to each other.

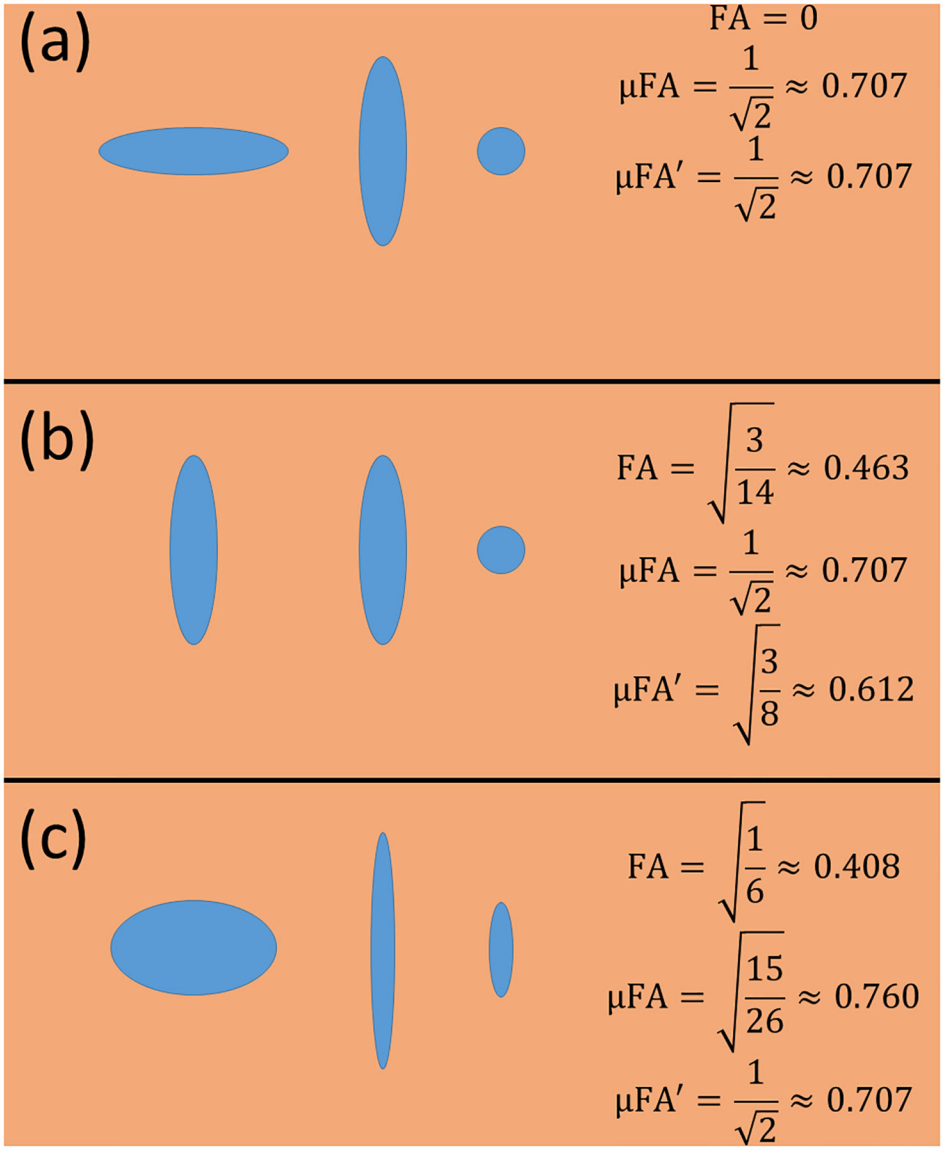

FIGURE 2:

Effect of symmetry transformations for a three compartment model with equal water fractions. (a) Each compartment's diffusion tensor has eigenvalues of (2,1/2,1/2). The principal eigenvectors of the leftmost, center, and rightmost diffusion ellipsoids (blue) are aligned, respectively, with the x-direction (horizontal), y-direction (vertical), and z-direction (perpendicular to image plane). FA is zero while μFA and μFA′ are equal. (b) After a rotation of the leftmost ellipsoid by 90° in the xy-plane, FA increases and μFA′ decreases, but μFA is unchanged. (c) If the global deformation of Equation 5 is applied to all three diffusion tensors instead of a local rotation, both FA and μFA increase, but μFA′ is unchanged. For the example shown, the deformation tensor **A** was set equal to one-half of the diffusion tensor for the center ellipsoid.

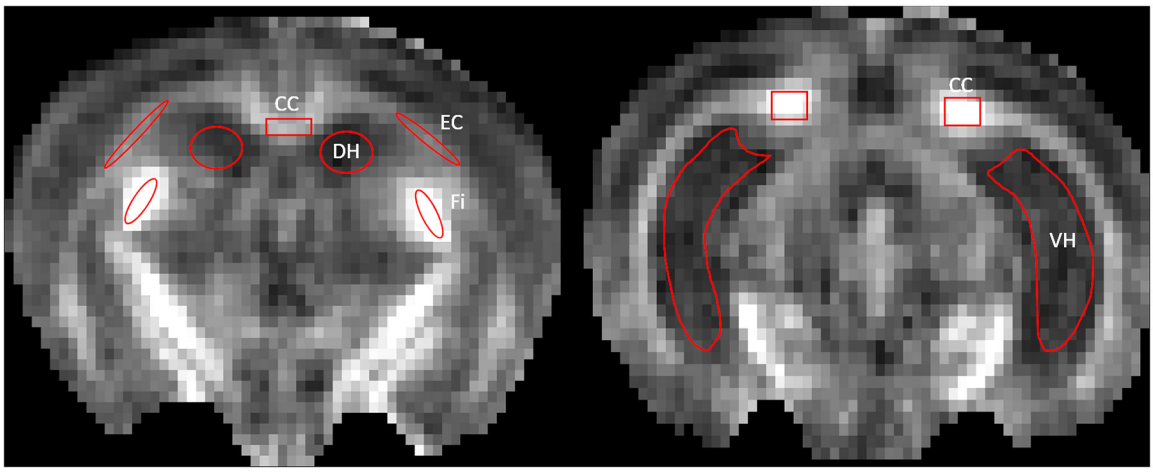

FIGURE 3:
Examples of regions of interest (ROIs) considered in this study outlined in red on FA maps from two coronal slices. Voxels from the left and right sides were pooled into a single ROI for each brain structure. Fi = fimbria, CC = corpus callosum, EC = external capsule, DH = dorsal hippocampus, VH = ventral hippocampus.

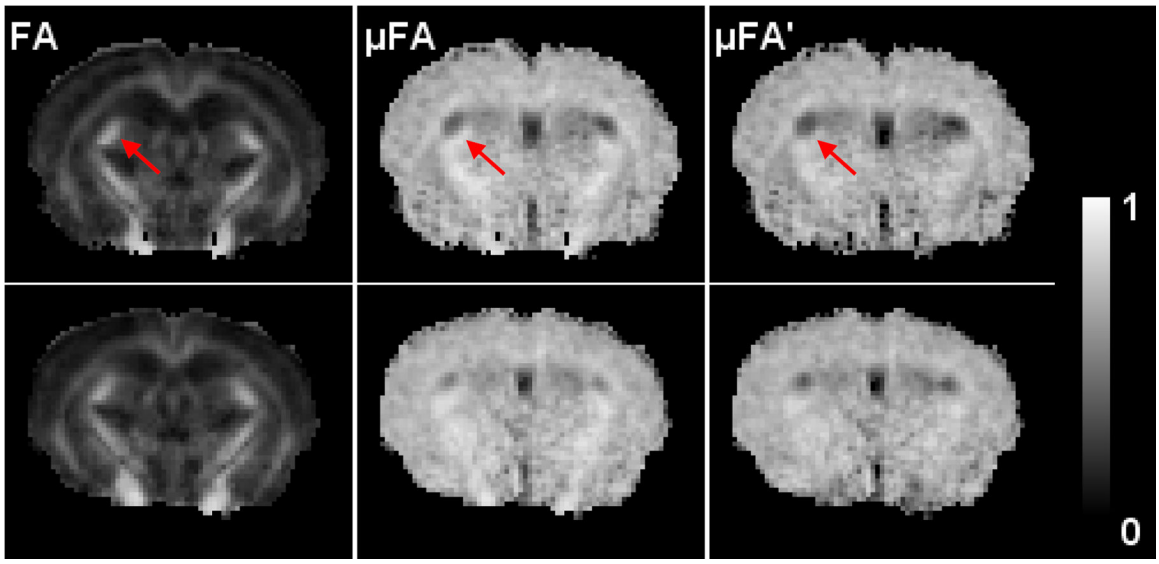

FIGURE 4:

Representative FA, μFA and μFA′ maps from a single coronal slice of 2 months old normal control (NC, first row) and transgenic (TG, second row) mice. Both types of MA are relatively large throughout most of the brain parenchyma including gray matter regions where FA is low. The μFA and μFA′ differ in that the former is also sensitive to macroscopic anisotropy while the latter is not. This can be seen, for example, in Fi (red arrows), where μFA is noticeably larger than μFA′ due to a substantial macroscopic contribution. Notice also that FA, μFA and μFA′ all have low values within the ventricles as expected for cerebrospinal fluid.

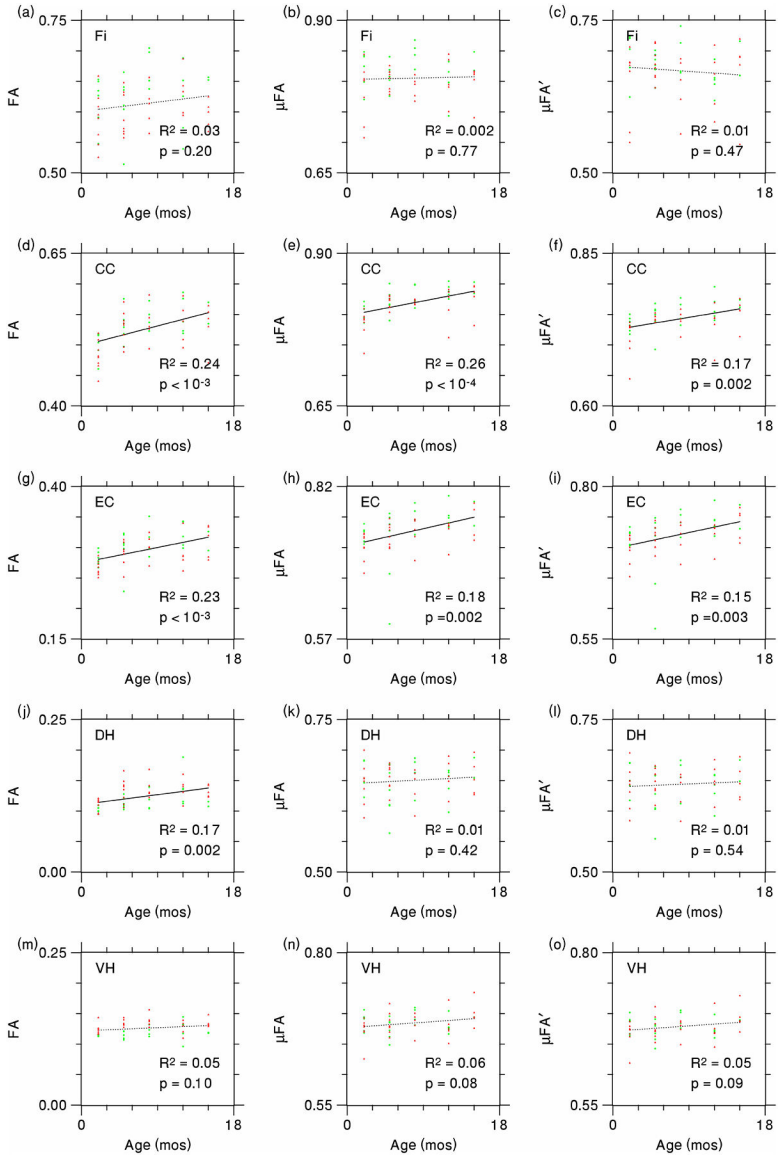

FIGURE 5:

FA, μFA and μFA′ for all animals and ROIs at all five time points (2, 5, 8, 12, and 15 months). Each data point is a separate animal. Green data points are for NC mice, and red data points are for TG mice. Linear regression lines are plotted for each ROI and anisotropy measure with the corresponding coefficients of determination (R^2) and p-values being indicated. The regression lines are for the pooled data from both types of mice, and significant correlations are indicated by solid lines ($p < 0.05$) while dotted lines denote insignificant correlations. All significant correlations had positive slopes showing that diffusion anisotropy increases with age. Note that the intervals for the vertical axes are all 0.25, but the minimum and maximum values vary according to ROI and anisotropy measure. Fi = fimbria, CC = corpus callosum, EC = external capsule, DH = dorsal hippocampus, VH = ventral hippocampus.

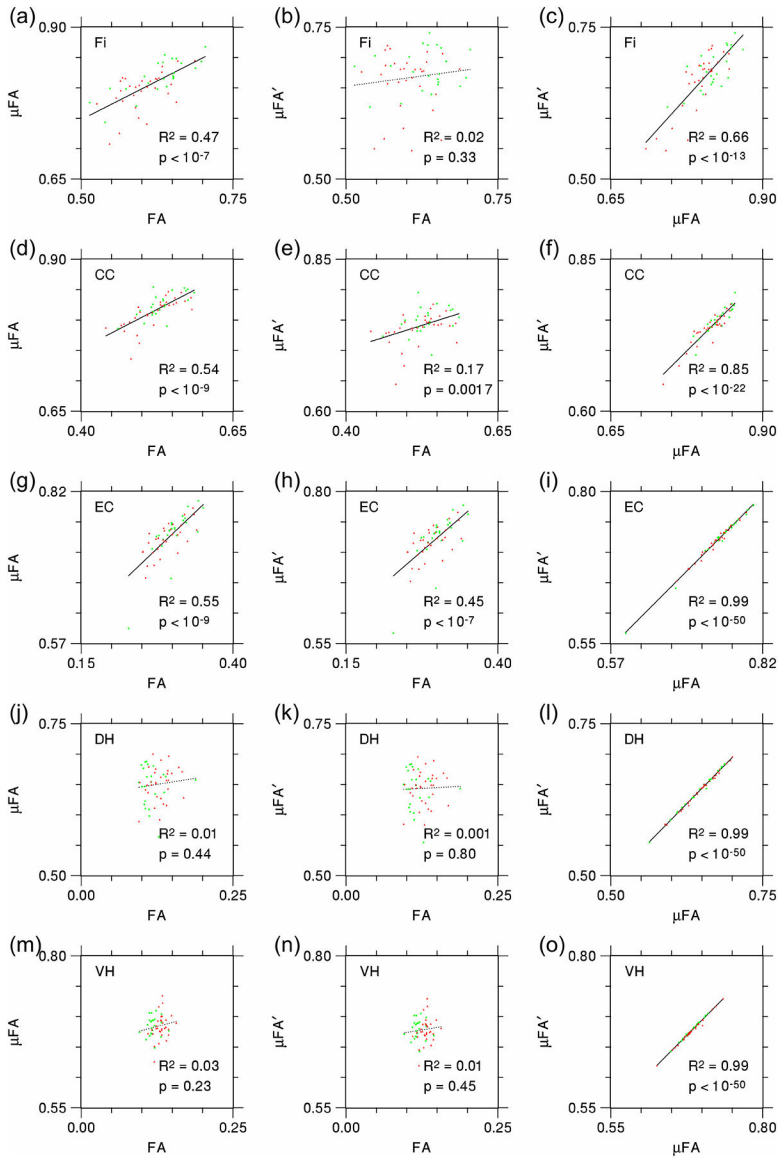

FIGURE 6:

Correlation plots for the three anisotropy measures from all animals and ROIs. Solid lines indicate significant correlations, and dotted lines are used for insignificant correlations. The μFA and μFA′ are strongly correlated in all ROIs, but FA is only significantly correlated with μFA in the Fi, CC, and EC and with the μFA′ with in the CC and EC. Green data points are for NC mice, and red data points are for TG mice. Note that the maximum and minimum of the axes vary with ROI and anisotropy measure. Fi = fimbria, CC = corpus callosum, EC = external capsule, DH = dorsal hippocampus, VH = ventral hippocampus.

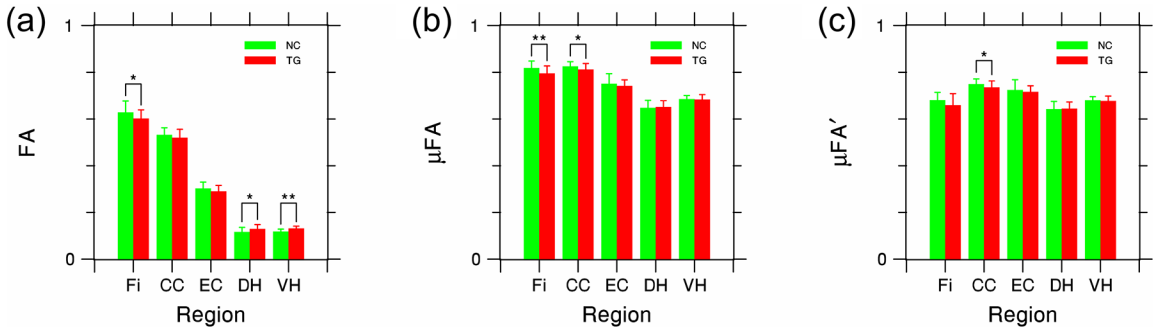

FIGURE 7:

Mean values for each anisotropy measure from all five ROIs. Data are pooled for all time points but separated by group. In all cases μFA′ > FA, revealing that MA is relatively more pronounced than macroscopic anisotropy. Group differences are small, but (uncorrected) p-values less 0.05 are found in 6 out of the 15 comparisons. The error bars indicate standard deviations. Fi = fimbria, CC = corpus callosum, EC = external capsule, DH = dorsal hippocampus, VH = ventral hippocampus. *$p < 0.05$, **$p < 0.01$.